

# Particle-In-Cell simulations of the filamentation process in magnetized radio-frequency plasmas

Huidong Huang<sup>1</sup> , Jian Chen<sup>1, 1</sup> , and Zhibin Wang<sup>1, 1</sup> 

<sup>1</sup> Sino-French Institute of Nuclear Engineering and Technology, Sun Yat-Sen University, Zhuhai 519082, People's Republic of China

E-mail: [chenjian5@mail.sysu.edu.cn](mailto:chenjian5@mail.sysu.edu.cn) and [wangzhib8@sysu.edu.cn](mailto:wangzhib8@sysu.edu.cn)

Received July 2024, revised April 2025

**Abstract.** In a uniform radio-frequency (RF) plasma between a large electrode pair, the addition of an axial magnetic field induces diverse longitudinal filaments. To reveal its pattern dynamics, we conduct two-dimensional (2D) Particle-In-Cell (PIC) simulations, capturing the entire evolution of the filamentation process. We found that the entire evolution experiences two dynamic stages. In the first stage, electrostatic standing waves and plasma density ripples grow synergistically, forming filamentary pattern. Our results show that the plasma ripples and RF electrostatic standing waves are modulated. In addition, each filament equips a double-humped peak. The spectrum reveals that the oscillations are mainly RF and its higher harmonics. Subsequently, the plasma shifts towards a dynamic regime governed by the competition between Lorentz and thermal pressure forces, characterized by the chaotic evolution of filaments. Through RF-cycle averaging, our force analysis demonstrated that electrons and ions are governed by the magnetic force and electric force respectively. The time-averaged magnetic force drives electrons to accumulate at plasma density maxima, while time-averaged electric force pushes ions into the same regions, jointly molding the filaments. These novel clues pave the way for a theoretical understanding of filamentation instability and provide essential references for effectively manipulating magnetized plasmas.

**Keywords:** pattern dynamics, magnetized plasma, radio-frequency discharge, Particle-In-Cell simulation

Submitted to: *Plasma Sources Sci. Technol.*

† Authors to whom any correspondence should be addressed.

## 1. Introduction

Magnetic fields are commonly utilized in gas discharges to enhance the plasma density [1, 2, 3] and modify plasma shape [4, 5, 6]. Particularly, people have shown a keen interest in magnetizing charged dusty plasmas because of the dust contamination problem in various plasma-related techniques [7, 8, 9]. Two decades ago, Konopka et al. introduced a strong magnetic field into an radio-frequency (RF) discharge chamber, initially aiming to study magnetized dusty plasmas. They discovered that RF plasmas subject to an axial magnetic field emerge filamentation, giving rise to a sequence of luminous patterns that extends along the magnetic field lines [10]. These patterns can manifest either as organized formations (like concentric rings) or irregularly-moving filaments lacking regularity [11, 12]. Remarkably, the experiments demonstrated that the filamentation can exhibit without dusts [10, 11, 12], thus it is a phenomenon inherent to pure plasma itself. However, these filamentary patterns can significantly influence the dust motion [11, 13, 14] (see [video](#)). This, in turn, offers novel possibilities for the dynamic control of industrial dust. Overall, studying filamentation in magnetized RF plasmas not only enhances our understanding of magnetized plasmas but also has promising implications for a variety of applications, including controlled fusion [15, 16], semiconductor etching [17, 18], surface modification [19] and material deposition [20].

Significant efforts have been devoted to experimental investigations of the filamentary patterns. Konopka and Schwabe et al. carried out the earliest observations on the formation of luminous filaments [10, 11] and they proposed that the filamentation strength depends on the magnetization of ions. Their findings also suggested that filamentation modifies dramatically the ion transport [11]. Subsequently, Thomas et al. extensively studied the filamentation in magnetized dusty plasmas [21, 22, 13, 12]. By varying the magnetic intensity, power deposition, and gas pressure, they established an empirical law for the filamentation strength. Recently, highly-resolving imaging [23] has further revealed the multi-morphology of the pattern micro-structure, varying with parameter changes. Results showed that the filaments undergo chaotic flowing, collective rotating and spinning (see [video](#)), showcasing the highly nonlinear filamentation pattern dynamics.

Besides experimental efforts, combined numerical–theoretical analysis has also been performed to unravel pattern formation mechanisms in magnetized RF plasmas. Menati et al. employed a two-dimensional hybrid model [24] to investigate the pattern formation of in a magnetized capacitively-coupled argon plasma between a RF-powered metal electrode and a grounded electrode with a dielectric barrier [25]. Simulation results showed the di-

electricity is strongly correlated with the filamentation strength. Afterwards, they employed a three-dimensional (3D) two-fluid model to reproduce the longitudinal plasma ripples akin to experimental observations [26]. Based on the simulation results, they considered the filamentary plasma to be generated due to diffusion [27]. However, they have recently reinterpreted these structures as Turing patterns [28], which has effectively revealed the magnetic field’s the crucial role in driving plasma filamentation.

Despite a substantial progress in revealing the mechanism of filamentary pattern formation, the understanding of the dynamics of filamentary plasmas is relatively limited. The primary motivation of this study is to comprehensively characterize the non-equilibrium dynamics of filamentary plasmas. We attempt to provide a kinetic perspective for the entire evolution of filamentation.

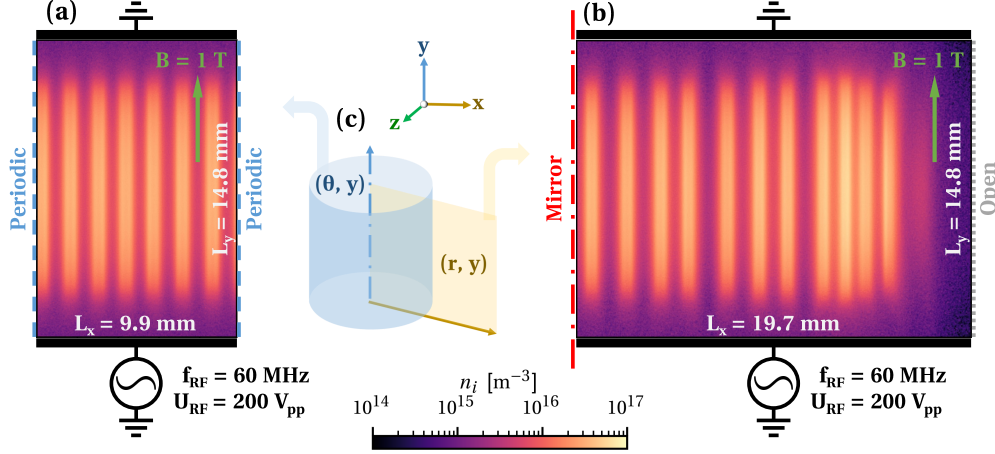
In this study, we conduct simulations of a magnetized argon RF discharge by employing a Particle-In-Cell/Monte-Carlo-Collision (PIC/MCC) method [29, 30, 31]. This simulation technique incorporates the electron and ion kinetics [32, 33, 34] as well as their neutral collisions [35, 36]. We segmented the whole process into two dynamic regimes, namely the standing wave growing (SWG) stage and the pattern evolving (PE) stage, and analyzed them separately. The multi-timescale analysis characterizes the RF cycle-averaged dynamics of the filamentary plasma. We have identified the key forces that govern the pattern dynamics, providing insight into the maintenance and evolution of filaments.

This paper is organized as follows: the employed simulation method are described in section 2. The results of the full evolution are presented and discussed in section 3, and a summary is provided in section 4. Additional supports are presented in the appendix.

## 2. Physical Models and Simulation Method

In this study, we adopt two distinct structures of two-dimensional (2D) planar simulation domain ( $L_x \times L_y$ ) with separately (a) periodic boundaries and (b) open boundaries, as sketched in figure 1. These two topologies are separately related to two orthogonal cross-sections,  $(\theta, y)$  and  $(r, y)$ , as shown in figure 1(c). Thus  $y$  signifies the axial coordinate, and  $x$  can represent either the azimuthal ( $\theta$ ) or the radial ( $r$ ) coordinate, with neglecting the limited effects of the geometric curvature, as shown in [37, 5, 38, 39].

- (a) Periodic boundaries. It is of size  $L_x \times L_y = 9.9 \text{ mm} \times 14.8 \text{ mm}$ . Periodic boundary conditions are used for the both left and right boundaries ( $x = 0$  and  $x = L_x$ ). The



**Figure 1.** Schematic diagrams of the simulation setups. The planar simulation domains with dimensions  $L_x \times L_y$  and (a) periodic boundaries, as well as (b) open boundaries, are considered to analyze (c) the cross-sections  $(\theta, y)$  and  $(r, y)$  respectively. Both cases are at simulation time  $t = 0.1$  ms, already reached quasi-steady state.

coordinate domain  $(x, y)$  should be regarded as the lateral surface  $(\theta, y)$  of a cylinder.

- (b) Open boundaries. It is of size  $L_x \times L_y = 19.7 \text{ mm} \times 14.8 \text{ mm}$ . A symmetry axis is defined at the left boundary ( $x = 0$ ), while the right boundary ( $x = L_x$ ) is left open. The coordinate domain  $(x, y)$  could be regarded as an arbitrary longitudinal section  $(r, y)$  with the axis as one side.

In both these two topologies, the plasma is immersed in axial external magnetic field  $|\mathbf{B}| = B_y = 1.0 \text{ T}$ ; the upper electrode at  $y = L_y$  is grounded, and the lower electrode located at  $y = 0$  is powered with an RF voltage. The RF voltage provides a sinusoidal waveform  $U(t) = U_0 \sin(2\pi f_{\text{RF}} t)$  with  $U_0 = 100 \text{ V}$  and  $f_{\text{RF}} = 60 \text{ MHz}$ . The domain is filled with argon as the background gas and only singly-charged  $\text{Ar}^+$  are considered in the simulations. Particles that hit these two electrodes are assumed to be absorbed. The vacuum permittivity  $\epsilon_0$  is applied to entire space and boundaries. The electrodes with positive permittivity differ from the actual ones, but this numerical setting was justified by [25].

We explored the filamentation process with periodic configuration (figure 1(a)) and the open configuration (figure 1(b)). As the quasi-steady state is reached, both configurations exhibit filaments of comparable structures, magnitudes ( $\max\{n_p\} \lesssim 1 \times 10^{17} \text{ m}^{-3}$ ) and scales (diameter of  $1.5 \pm 0.1 \text{ mm}$ )<sup>2</sup>, which suggests boundary conditions (periodic vs. open) impose relatively limited effects on the filament's structure. These observations demonstrate that the filamentation phenomenon exhibits cross-configuration robustness. Hence, for simplicity, we select the periodic configuration to illustrate the pattern formation and nonlinear dynamics.

<sup>‡</sup> In our simulations, the FWHM (full width of half maximum) of plasma density ripple is  $\sim 1 \text{ mm}$ , which is consistent to the range ( $w_{\text{fil}} \approx 1 \text{ mm}$ ) reported in the experiments [10, 11, 12, 23].

In these models, the external circuit is not considered. This is because both directly-coupled [10] and capacitively-coupled [25, 12] discharges have been experimentally demonstrated to exhibit filamentation, i.e., the blocking capacitor is not a necessary complexity for the occurrence of this phenomenon.

All the simulations in this study are performed using an open-source PIC/MCC code named EDIPIC-2D. EDIPIC-2D has been well benchmarked against multiple codes [38] and has been successfully applied to numerous low-temperature plasma simulations, as recently reported in the literature [40, 41, 42]. Note that although the code is 2D in position space, it is 3D in velocity space.

These simulations start with a uniform plasma with the plasma density  $n_{p,0} = n_{e,0} = n_{i,0} = 2.5 \times 10^{16} \text{ m}^{-3}$ , the electron temperature  $T_{e,0} = 3.0 \text{ eV}$  and the ion temperature  $T_{i,0} = 0.026 \text{ eV}$ . The background gas is argon and its pressure is fixed as  $6.0 \text{ Pa}$ . Initially, 500 super-particles per cell for each species are created, with the particle weight  $w = 73728$ . After dozens of microseconds, these systems ultimately reaches a quasi-steady state. As exemplified in figure A1, regardless of whether the  $n_{p,0}$  is set to  $1 \times 10^{14} \text{ m}^{-3}$ ,  $2.5 \times 10^{16} \text{ m}^{-3}$  or  $1 \times 10^{17} \text{ m}^{-3}$ , the number of super-particles eventually converges to a narrow range, suggesting that the minimal effects of initial parameters on the quasi-steady state.

Three types of electron-neutral collisions, namely, elastic scattering, excitation and ionization, as well as  $\text{Ar}^+$ -Ar charge exchange collisions are included. The cross-section data used in the simulations are taken from [43, 44, 45, 46]. The secondary electron emission (SEE) [47] is disabled in the present work, because SEE has a limited impact on the filamentation process (see the results shown in figure A2 of Appendix A, which are consistent with the findings in [25]).

The spatial grid size and time step used in the simulation were carefully selected. The cell size  $\Delta x = \Delta y = 38.4 \mu\text{m}$  is able to capture the Debye wavelength  $\lambda_{D_e}$  and the ion Larmor radius  $r_{L_i}$

( $r_{Li} = 144 \mu\text{m}$  and  $\lambda_{De}$  are on the order of 0.1 mm). Resolving electron Larmor radius ( $r_{Li} = 6 \mu\text{m}$ ) requires a smaller cell size and leads to an unaffordable computation cost. Since the characteristic width of the filaments (1.4 mm) is much larger than the electron Larmor radius, we neglect the finite electron Larmor radius effects [48, 49, 50] on the filamentation process. The time step  $\Delta t = 18.7 \text{ ps}$  is certain to resolve the electron plasma frequency  $f_{pe} \lesssim 3 \text{ GHz}$  as well as the radio-frequency  $f_{RF} = 60 \text{ MHz}$ . To simulate the slow motion of filaments, the simulation was run for 1 ms (53 million time-steps).

### 3. Simulation Results and Discussions

In our simulations, the RF plasmas exhibit filamentation under a strong axial magnetic field, yet the filaments disappear at 0 T. These results align with experimental observations [11, 13] and numerical results [25].

Our simulation results indicate that the entire evolution of plasma filamentation can be subsumed into two developmental phases: the standing wave growing (SWG) stage and the pattern evolving (PE) stage.

- I. The standing wave growing (SWG) stage encompasses pattern initiation and amplification. In this stage, the transverse RF electrostatic standing wave and plasma filaments emerge from a uniform background.
- II. The pattern evolving (PE) stage represents a chaotic stage during the entire evolution. At this stage, the plasma filaments can flow erratically, merge in pairs or even surge suddenly from depletion region.

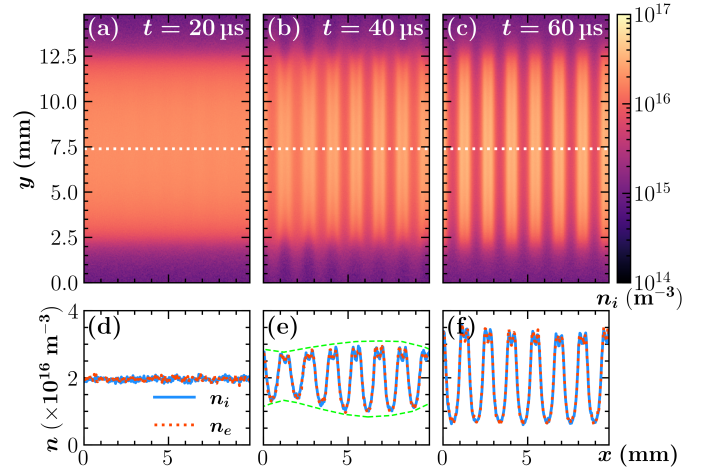
Once the pattern reaches saturation, the filamentary plasma transitions from the SWG stage to the PE stage.

In the following two sub-sections, we will analyze these two stages separately. In this paper, we aim to provide a panoramic view to the entire filamentation process, rather than elaborating on the RF dynamics details (cf. the supplemental videos <sup>3</sup>).

#### 3.1. Standing Wave Growing Stage

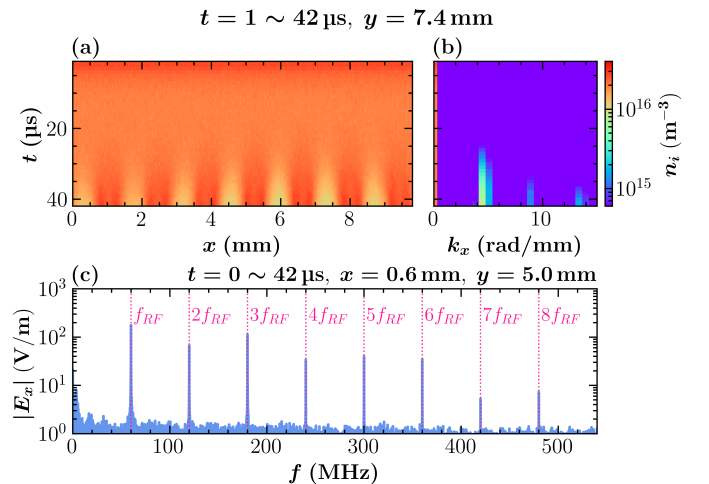
Figure 2 shows the evolution of the ion density distributions in the SWG stage. Figures 2(a–c) depict the ion density distribution at 20  $\mu\text{s}$ , 40  $\mu\text{s}$  and 60  $\mu\text{s}$ , while figures 2(d–f) show the corresponding ion density distribution along the mid-plane ( $y = 7.4 \text{ mm}$ ), denoted by the white lines in figures 2(a–c). As shown in figure 2(a), ion density keeps relatively uniform in the first 20  $\mu\text{s}$  in the bulk region. Two RF sheaths are formed near the upper and lower electrodes with the thickness around 2 mm. The center plasma density is about  $2 \times 10^{16} \text{ m}^{-3}$ . Subsequently, horizontal disturbances surge from uniform background, leading to the rippled structures, as depicted in figures 2(b) and 2(c). These ripples maintain coherent structures that resembles the filaments observed in experiments [11, 12].

As seen in figures 2(d–f), the magnitude of density perturbation keeps growing, during which quasi-neutral



**Figure 2.** Standing wave growing stage. The  $\text{Ar}^+$  2D profiles present the plasma distribution at distinct moments:  $t =$  (a) 20  $\mu\text{s}$ , (b) 40  $\mu\text{s}$ , (c) 60  $\mu\text{s}$ . The white dot-dashed lines highlight the half-height altitude  $y = 7.4 \text{ mm}$ . Blue and red curves indicating respectively  $\text{Ar}^+$  and  $e^-$  depicted in (d–f) are their corresponding 1D profiles along the half-height slice. Typical modulational feature manifests on the plasma ripples in (e), which is enveloped by lime dashed curves.

condition is still fulfilled (electron and ion densities are almost equal). Interestingly, as depicted in figures 2(e) and 2(f), the shape is clearly modulated, exhibiting an envelope structure (denoted by the lime dashed curves). Note that modulated envelopes exist in the electric field as well. Modulated waveform like this are often associated with parametric instabilities [51, 52, 53, 54]. In addition, each filament has an apparent double-humped structure, and intense RF electric field also exists on the inner side of these double-humped structures. These double-humps may be caused by intense charge separation [55].



**Figure 3.** Fourier spectra of SWG stage. (a) shows the half-height slice of the density varying over time, characterizing the SWG stage. (b) is its wavenumber spectrum evolving over time. Frequency spectrum (c) records the temporal Fourier transform of horizontal electric field  $E_x$ , measured by a probe at position ( $x = 0.6 \text{ mm}$ ,  $y = 5.0 \text{ mm}$ ). The time window of sampling extends from 0  $\mu\text{s}$  to 42  $\mu\text{s}$ . The characteristic frequencies are numerically well matched to the RF wave and its higher harmonics.

<sup>3</sup> See Supplemental Material [url] for more details on the RF dynamics.

Figure 3(a) displays the ion number density evolution within the transformed time window  $t = 1 \sim 42 \mu\text{s}$  at the slice  $y = 7.4 \text{ mm}$ , and figure 3(b) illustrates the corresponding wavenumber spectrum varying with time. The horizontal uniformity has been maintained until  $t = 30 \mu\text{s}$ , from which moment observable disturbances emerge. Seven filaments form gradually with high regular shapes and nearly equal diameters. The transverse wavelength of these wave packets is  $\lambda_x = 1.4 \text{ mm}$ , i.e.  $k_x = 2\pi/\lambda_x = 4.49 \text{ mm}^{-1}$ , as depicted in figure 3(b). Figure 3(c) shows the spectrum of the horizontal component of  $\mathbf{E}$  at position ( $x = 0.6 \text{ mm}$ ,  $y = 5.0 \text{ mm}$ ). Result shows that the characteristic frequencies are exact  $f_{\text{RF}} = 60 \text{ MHz}$  and its higher harmonics.

During SWG stage, multiple parameters at various areas are examined, including densities, temperatures, velocities, current flux, electrostatic potential, electric fields, etc. Our results show that these parameters share same characteristic frequency spectrum depicted in figure 3(c), regardless of probe location. In these spectra, one can merely observe the characteristic peaks of RF ( $f_{\text{RF}} = 60 \text{ MHz}$ ) and its harmonics. This spectral pattern highlights the the predominant role of RF pumping. This suggests that the cyclotron waves and hybrid waves in this context are negligible, since plasma frequencies  $f_{pe} = 1 \sim 3 \text{ GHz}$  and  $f_{pi} \approx 4.6 \text{ MHz}$ , cyclotron frequencies  $f_{ce} = 28 \text{ GHz}$  and  $f_{ci} = 0.4 \text{ MHz}$ . To conclude, the standing wave is solely excited by RF pumping wave. This spectral pattern may originate from resonance [56] or modulation [57, 41] of RF components. However, in RF discharge experiments, standard detection systems typically filter out RF harmonics, which may mask their existence.

It should be noted that the periodic configuration has eliminated extrinsic disturbances, such as asymmetric reactor structure in real experiments [25] and lateral plasma sheaths [25, 28]. Hence, the occurrence of  $E_x$  standing wave should be intrinsic.

In conventional consideration, axial RF pumping should have produced merely a longitudinal wave, but here a transverse wave appears. Therefore, there should exist a transverse wave mode that allows mode conversion from RF longitudinal wave. The wave mode in which the RF pumping engages is still a challenge to determine, since  $f_{\text{RF}} = 60 \text{ MHz}$  differs far from the frequency band of the usual waves.

These results show that the filamentary plasma is an inherently complex system. The self-organization process engages multiple competing mechanisms. According to [26, 27, 28], an two-fluid diffusion model realized plasma filamentation within a 3D zero-Dirichlet box, despite the exclusion of RF pumping. Recent work [28] described these filamentary structures as Turing patterns through an activator-inhibitor framework [58]. This phenomenological perspective has rather effectively delineated the important role of magnetic field in initiating charge separation and inhomogeneous discharge. However, in contrast to the activation-inhibition-diffusion hypothesis recommended in [28], our simulations do not include the ion-electron recombination effect as inhibition.

Besides Turing instability, there are other factors potentially related to the pattern formation. As a nonlinear system, RF discharge itself encompasses multiple complexities, such as RF-induced charge separation, RF heating, gas ionization, wave non-linearities, etc. [59] For instance, modulated ripples are often associated with modulational instabilities [54, 60]. Other underlying instabilities, like Kelvin–Helmholtz instabilities in magnetized plasmas and drift instabilities in inhomogeneous plasmas [61], may also contributed to the growth of plasma ripples.

Furthermore, simulations [26, 28] suggest that the filamentation phenomenon is not solely attributable to RF discharge and exhibits broader universality. Perhaps, filamentation may occur in other working conditions, such as direct-current discharge [62]. This is a topic warranting further exploration.

### 3.2. Pattern Evolving Stage

In the pattern evolving (PE) stage, the plasma transits to non-equilibrium dynamical system. The filaments can flow erratically, merge in pairs or even surge suddenly from depletion region, suggesting their highly nonlinear nature. Regularity is disrupted as the number and positioning of filaments no longer remain constant. Yet filaments maintain nearly equal diameters and amplitudes of the same order.

Although the filaments flow chaotically, pattern dynamics tend to favor the coalescence of filaments into a smaller number yet with stronger magnitude. Our simulation stabilizes at around 4 filaments. Throughout the PE stage, filamentary plasma exhibits quasi-steady oscillations over a  $0.1 \mu\text{s}$  cycle but never attains a true steady-state.

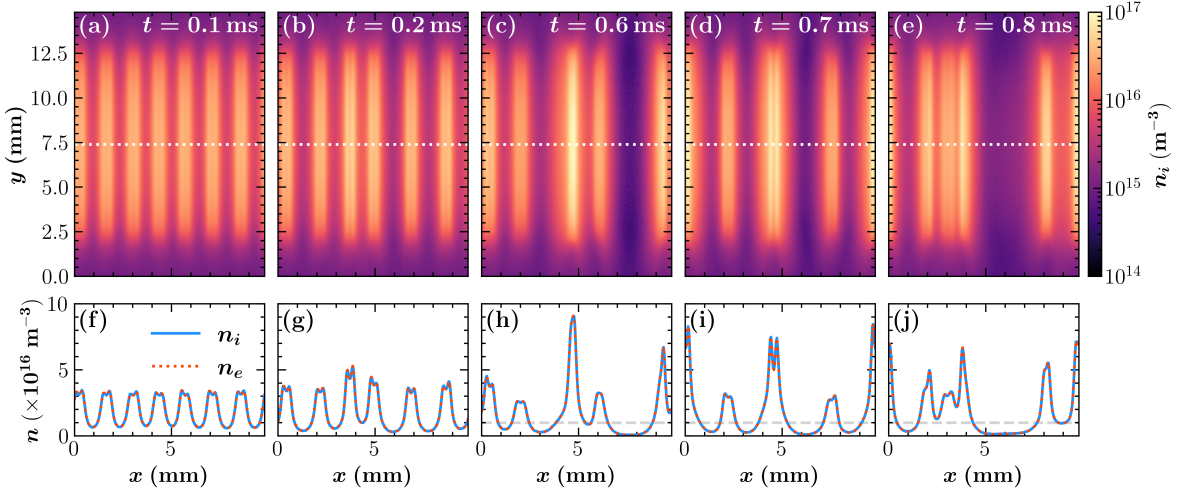
Now, we focus on the time-averaged effects of RF dynamics and use operator  $\langle \rangle$  to denote the time-averaging over multiple RF-periods. We define for any quantity  $\clubsuit$ ,

$$\langle \clubsuit \rangle(\mathbf{x}, t) = \tau^{-1} \int_{t-\tau/2}^{t+\tau/2} \clubsuit(\mathbf{x}, t') dt',$$

with duration  $\tau = 6T_{\text{RF}} = 0.1 \mu\text{s}$ .

At the microsecond scale, the time-averaged density  $\langle n_s \rangle$  remains basically unchanged. However, it can be observed that new plasma filaments occasionally emerges from the depletion region (e.g., in figure 5(a)), owing to high local ionization rate and magnetic-confined horizontal transport.

Figure 4 shows the plasma density snapshots in the PE stage. Two groups of sub-figures 4(a–b) and sub-figures 4(c–e) present separately the transition from SWG to PE stage and a highly chaotic scenario. Their corresponding density curves are plotted in sub-figures 4(f–j) respectively. At  $0.1 \text{ ms}$ , seven filaments are regularly arranged (figure 4(a)) and their density peak are of equal height (figure 4(f)); But at  $0.2 \text{ ms}$ , only six irregular filaments distribute erratically (figure 4(b)), their density values start to differ as well (figure 4(g)). Such transition is attributed to the motion and pairwise merging of filaments. Having experienced a characteristic evolution time about  $0.1 \text{ millisecond}$ , a pair of filaments meld into single one, the charged particle numbers



**Figure 4.** Pattern evolving stage. The  $\text{Ar}^+$  2D profiles present the plasma distribution at distinct moments:  $t =$  (a) 100 ms, (b) 200 ms, (c) 600 ms, (d) 700 ms, (e) 800 ms. The white dot-dashed lines highlight the half-height altitude  $y = 7.4$  mm. Blue and red curves indicating respectively  $\text{Ar}^+$  and  $e^-$  depicted in (f–j) are their corresponding 1D profiles along the half-height slice. The grey dashed line in (h–j) is the density level of  $1 \times 10^{16} \text{ m}^{-3}$ , as a criterion to distinguish regions of filament or depletion.

stack up, a brighter filament is left, as clearly drawn in figures 4(f–g). Next, the scenario projected onto figures 4(c–e) shows a representative instance of chaotic hydro-kinematics, depicted through the evolution of the ion distribution during time slot  $t = 0.6 \sim 0.8$  ms, capturing various phenomena including chaotic flowing, pairwise merging, sudden emerging and wave saturating. At these moments, some packets flow together and locate close enough to dynamically view them as a whole.

The plasma densities of the filament and the depletion region differ greatly. Typically, in depletion regions, the plasma density is below  $1 \times 10^{16} \text{ m}^{-3} =: n_c$ , thus we define this density level as a criterion for demarcating the filament and depletion regions. A contiguous region with  $n_i > n_c$  is regarded as a filament.

Figure 4(c) initially captures five filaments with irregular spatial positioning and distinct peak-density. During fully nonlinear development (figure 5(a)), the plasma aggregates towards three brightest filaments in 4(e). A characteristic “sudden emerging” event occurs in figure 4(d), where the second rightmost filament abruptly materializes from the depletion zone at 0.66 ms (figure 5(a)). This transient phenomenon initiates without observable precursors in prior frames (figure 4(c)), exhibiting sudden onset and rapid progression.

To analyze the non-equilibrium pattern dynamics, we commence with a two-fluid model of magnetized cold plasma. The complete fluid momentum balance equation for charged species in cold plasma is composed of six mechanical terms, namely,

- (a) inertia  $\partial_t m_s n_s \mathbf{U}_s$ ,
- (b) convection  $\mathbf{f}_s^{\text{conv}} = -(\mathbf{U}_s \cdot \nabla) m_s n_s \mathbf{U}_s$ ,
- (c) thermal pressure  $\mathbf{f}_s^{\text{th}} = -k_B \nabla \cdot n_s \hat{\mathbf{T}}_s$ ,
- (d) gyro-viscosity  $\mathbf{f}_s^{\text{gyro}} = -\nabla \cdot \hat{\Pi}_s^{\text{gyro}}$ ,
- (e) neutral collision  $\mathbf{f}_s^{\text{n}} = -m_s n_s \nu^{s-n} \mathbf{U}_s$ ,
- (f) electromagnetism  $\mathbf{f}_s^{\text{em}} = q_s n_s (\mathbf{E} + \mathbf{U}_s \times \mathbf{B})$ .

These are based on what’s described in the textbooks [63, 61, 55] and literature [64, 50, 42]. Here, the gyro-viscosity  $\hat{\Pi}_s^{\text{gyro}}$  [65] contributes the major component of the shear stress, with due consideration of the Finite Larmor Radius effect [66, 50]. The formalism for numerical calculation of gyroviscosity tensor  $\hat{\Pi}_s^{\text{gyro}}$  ultimately adopted the widely used formulation outlined respectively in [50], consistent with that detailed in [42]. In addition, the major type of collision between the cold plasmas and static neutral background is the neutral collision term [55] under the neutral collision frequency  $\nu^{n-s}$ . The momentum equation is thus

$$\partial_t m_s n_s \mathbf{U}_s = \mathbf{f}_s^{\text{conv}} + \mathbf{f}_s^{\text{th}} + \mathbf{f}_s^{\text{gyro}} + \mathbf{f}_s^{\text{n}} + \mathbf{f}_s^{\text{em}}. \quad (1)$$

The time-averaged convection  $\langle \mathbf{f}_s^{\text{conv}} \rangle$  is estimated by the ponderomotive force  $\mathbf{f}_s^{\text{pm}}$  i.e.  $\langle \mathbf{f}_s^{\text{conv}} \rangle \approx \mathbf{f}_s^{\text{pm}}$ . This approximation arises by substituting the dispersion relation into the expression for the convective force

$$\langle \mathbf{f}_s^{\text{conv}} \rangle = -m_s \langle n_s (\mathbf{U}_s \cdot \nabla) \mathbf{U}_s \rangle \approx -\frac{1}{2} m_s \langle n_s \rangle \nabla \langle \mathbf{U}_s^2 \rangle,$$

which ultimately yields the electrostatic ponderomotive force [67, 68, 69]

$$\mathbf{f}_s^{\text{pm}} = -\frac{\langle n_s \rangle q_s^2}{4m_s} \nabla \left\langle \frac{E_{\perp}^2}{\omega^2 - \omega_{cs}^2} + \frac{E_{\parallel}^2}{\omega^2} \right\rangle,$$

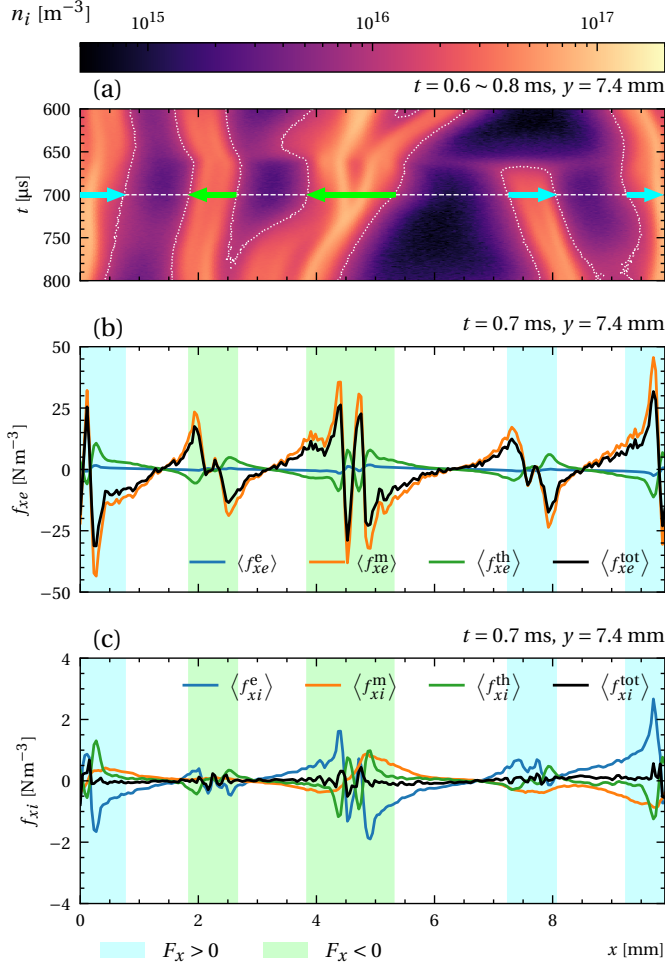
where  $\omega_{cs}$  is the cyclotron frequency,  $\omega$  is the wave frequency, and the electric field components  $E_{\perp}$  and  $E_{\parallel}$  are perpendicular and parallel to the magnetic field  $\mathbf{B}$ , respectively. Term  $\langle \mathbf{E}^2 \rangle$  is slowly varying in the PE stage, thus time-derivative term of the ponderomotive force [70, 71, 72] is neglected. Contributions from anisotropic temperature [73] and non-local properties [74, 75] are also disregarded.

The time-averaged Lorentz force  $\langle \mathbf{f}_s^{\text{em}} \rangle = \langle \mathbf{f}_s^{\text{e}} \rangle + \langle \mathbf{f}_s^{\text{m}} \rangle = q_s \langle n_s \mathbf{E} \rangle + q_s \langle n_s \mathbf{U}_s \rangle \times \mathbf{B}$  sees the time-averaged fields  $\langle n_s \mathbf{E} \rangle$  and  $\langle n_s \mathbf{U}_s \rangle$  where the high frequency oscillations are filtered out by time-averaging. Via the same method, we calculate

the time-averaged values of thermal pressure force  $\langle \mathbf{f}_s^{\text{th}} \rangle = -k_B \nabla \cdot \langle n_s \hat{\mathbf{T}}_s \rangle$ , gyroviscous force  $\langle \mathbf{f}_s^{\text{gyro}} \rangle = -\nabla \cdot \langle \hat{\mathbf{\Pi}}_s \rangle$ , and neutral collisional friction  $\langle \mathbf{f}_s^{\text{n}} \rangle = m_s \langle n_s \mathbf{U}_s \rangle \nu^{n-s}$ . The time-averaged right-hand side of equation (1) is finally

$$\langle \mathbf{f}_s^{\text{tot}} \rangle = \mathbf{f}_s^{\text{pm}} + \langle \mathbf{f}_s^{\text{th}} \rangle + \langle \mathbf{f}_s^{\text{gyro}} \rangle + \langle \mathbf{f}_s^{\text{n}} \rangle + \langle \mathbf{f}_s^{\text{em}} \rangle, \quad (2)$$

where  $\langle \mathbf{f}_s^{\text{tot}} \rangle$  represents the effective resultant force, averaged over duration  $\tau = 0.1 \mu\text{s}$ , experienced by local fluid element.



**Figure 5.** Fluid dynamics of PE stage. The half-height slices constitute (a) the Ar<sup>+</sup> density profile varying over time  $t = 0.6 \sim 0.8$  ms, which displays the hydro-kinematics of PE stage. White dot-dashed contours close the regions of ion density exceeding  $1 \times 10^{16} \text{ m}^{-3}$  where are viewed as plasma filaments. In (a), the rightward cyan or leftward lime arrow attached upon each filament indicates the direction of total force  $F_x$  acting on whole filament at the moment  $700 \mu\text{s}$ . (b) and (c) demonstrate the local volume forces along the waistline  $y = L_y/2$  at  $700 \mu\text{s}$ , including the time-averaged resultant forces ( $\langle f_{xe}^{\text{tot}} \rangle$  and  $\langle f_{xi}^{\text{tot}} \rangle$ , black curves) and three kinds of dominant forces, that is, the time-averaged electrical force ( $\langle f_{xe}^e \rangle$ , blue curve), the time-averaged magnetic force ( $\langle f_{xe}^m \rangle$ , orange curve), and the time-averaged thermal pressure force ( $\langle f_{xe}^{\text{th}} \rangle$ , green curve) exerted upon electrons and ions. In both (b) and (c), lime or cyan patch spanning entire region of each filament, means that the total force acting on the whole filament is pointing to left-hand-side or right-hand-side, respectively.

Figure 5(a) presents the patterns flowing over time  $t = 0.6 \sim 0.8$  ms and the direction of the total force acting on each filament at  $t = 0.7$  ms. This scenario has been projected its moments  $t$

$= 0.6, 0.7, 0.8$  ms onto figures 4(c–e). Various phenomena including (i) chaotic flowing, (ii) pairwise merging, (iii) sudden emerging and (iv) wave saturating are clearly captured here. White dot-dashed curves enclose the regions of ion density exceeding  $n_c = 1 \times 10^{16} \text{ m}^{-3}$  where are tagged as filament areas for the force calculation.

The total force in the  $x$ -total, denoted as  $F_x$ , acting on each filament, is defined as the spatial integral of the horizontal component of the local total force  $\langle \mathbf{f}_{ix}^{\text{tot}} \rangle + \langle \mathbf{f}_{ex}^{\text{tot}} \rangle$  acting on each filamentary region

$$F_x = \int_{\text{filament region}} \langle f_{ex}^{\text{tot}} + f_{ix}^{\text{tot}} \rangle dx dy.$$

If  $F_x > 0$ , the total force  $F_x$  is directed to the right; if  $F_x < 0$ , the total force  $F_x$  is directed to the left.

The direction of  $x$ -resultant force acting on whole filament  $F_x$  at moment  $t = 0.7$  ms is indicated by the colored arrows overlaid on the background in figure 5(a). Here, the acceleration of each filament is in the same direction as the calculated resultant force  $F_x$  acting on it. Figure 5(b) displays the calculated result details of effective volume forces acting along the half-height level  $y = L_y/2$  at the moment  $t = 0.7$  ms. It includes the local total force ( $\langle f_{xe}^{\text{tot}} \rangle$ , shown as the black curve) and three dominant forces: the  $\langle f_{xe}^e \rangle$ ,  $\langle f_{xe}^m \rangle$  and  $\langle f_{xe}^{\text{th}} \rangle$ . In addition, a lime or cyan patch spanning the entire region of each filament indicates that the area total force  $F_x$  acting on the whole filament is directed towards the left-hand side or right-hand side, respectively. Figure 5(c) has the same format as figure 5(b), but it shows the force conditions of ions.

Around the simulation time  $t = 0.7$  ms, within a time interval of  $\pm 1 \mu\text{s}$ , the plasma near the half-height line  $y = L_y/2$  are regarded quasi-steady. However, on the scale of 100 microseconds, one can observe that the filamentary or rod-shaped flow clusters exhibit obvious collective speed changes. Thus, we calculate the force acting on the system at this moment and compare it with the simulation results. The force characteristics of electrons are summarized as follows: (i)  $\langle \mathbf{f}_e^{\text{tot}} \rangle$  is not balanced and contributes the largest share to  $F_x$ ; (ii) More specifically,  $\langle \mathbf{f}_e^m \rangle$  contributes the largest share to  $\langle \mathbf{f}_e^{\text{tot}} \rangle$ , followed by  $\langle \mathbf{f}_e^{\text{th}} \rangle$ , and then comes  $\langle \mathbf{f}_e^e \rangle$ ; (iii)  $\mathbf{f}_e^{\text{pm}}$ ,  $\langle \mathbf{f}_e^{\text{gyro}} \rangle$  and  $\langle \mathbf{f}_e^{\text{n}} \rangle$  are at least three orders of magnitude smaller than  $\langle \mathbf{f}_e^{\text{th}} \rangle$ , therefore neglected; (iv) The trend generally shows that  $\langle \mathbf{f}_e^{\text{th}} \rangle$  and  $\langle \mathbf{f}_e^e \rangle$  jointly resist  $\langle \mathbf{f}_e^m \rangle$ ; (v)  $\langle \mathbf{f}_e^{\text{tot}} \rangle$  transports electrons along the density gradient  $\partial_x n_p$ .

Then, we compared the force profiles of ions and electrons and found that: (i)  $\langle \mathbf{f}_i^{\text{em}} \rangle = \langle \mathbf{f}_i^e \rangle + \langle \mathbf{f}_i^m \rangle$  and  $\langle \mathbf{f}_i^{\text{th}} \rangle$  are nearly in balance; (ii) The maximum magnitude of  $\langle \mathbf{f}_i^{\text{tot}} \rangle$  is  $\leq 5\%$  of that of  $\langle \mathbf{f}_e^{\text{tot}} \rangle$ ; (iii)  $\mathbf{f}_i^{\text{pm}}$ ,  $\langle \mathbf{f}_i^{\text{gyro}} \rangle$  and  $\langle \mathbf{f}_i^{\text{n}} \rangle$  are also very small and thus neglected; (iv) The curve shape of  $\langle \mathbf{f}_i^{\text{th}} \rangle$  are highly similar to  $\langle \mathbf{f}_e^{\text{th}} \rangle$ ; (v) The directions of  $\langle \mathbf{f}_i^e \rangle$  and  $\langle \mathbf{f}_i^m \rangle$  are opposite to those forces acting on electrons, respectively.

Remarkably,  $\langle \mathbf{f}_e^m \rangle$  and  $\langle \mathbf{f}_i^m \rangle$  reveal that  $\langle E_x \rangle$  generate strong  $\langle E \rangle \times B$  shear flows twist around each plasma filament. The  $\langle U_{ez} \rangle$  in the depletion region is much larger than  $\langle U_{ex} \rangle$ . This flow may be an important factor in the formation of filamentary structures, for example, it could fragment plasma into small spots. This  $E \times B$  shear flow is a common feature in plasma

filamentation, and its existence was already implied in previous experimental observations [11, 23].

These results reveal that the total force  $\langle \mathbf{f}_e^{\text{tot}} + \mathbf{f}_i^{\text{tot}} \rangle$  are not balanced within the bulk plasma. In other words, the inertia term is always non-zero, which argues that the plasma of PE stage is far from a force-balanced system. The time-averaged thermal pressure force  $\langle \mathbf{f}_s^{\text{th}} \rangle$  and the time-averaged Lorentz force  $\langle \mathbf{f}_s^{\text{em}} \rangle$  significantly larger than the other three forces (by three orders of intensity at least). Therefore, these two forces are sufficient to approximate the resultant force acting on the plasma. The thermal pressure force  $\langle \mathbf{f}_s^{\text{th}} \rangle$  and the Lorentz force  $\langle \mathbf{f}_s^{\text{em}} \rangle$  are oriented in the inverse direction locally, which eventually drives the particles towards higher-density areas. At a larger scale, the total force  $F_x$  acting on each filament propels its integral motion in a manner similar to rigid body.

#### 4. Conclusions

In this study, we utilized 2D PIC/MCC simulations to investigate the filamentation process of magnetized RF plasma and analyze the associated pattern dynamics.


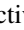
We observed two dynamic regimes in the complete filamentation process. Initially, longitudinal filaments emerge from a uniform background and amplify until saturation. Thereafter, filaments can flow, grow, merge, and emerge suddenly from depletion regions.

Our results show that the plasma ripples and RF electrostatic standing waves are modulated. Moreover, each filament equips a double-humped peak; intense RF electric field occurs inside these structures. The spectrum demonstrates that the oscillations are generally of multiple-RF frequencies.

Analysis of different terms of fluid momentum equation reveals that time-averaged forces such as Lorentz and thermal pressure dominate during the Pattern Evolving stage. The competition between electrical, magnetic and thermal pressure forces governs the motions of filaments. Through RF-cycle averaging, our analysis demonstrated that electrons and ions are governed by the magnetic force and electric force respectively. The time-averaged magnetic force drives electrons to accumulate at plasma density maxima, while time-averaged electric force pushes ions into the same regions, jointly molding the filaments.

These novel insights offer valuable guidance for future investigations into pattern dynamics and essential reference for effective manipulations of industrial plasmas. Our findings can provide the knowledge regarding the background magnetized plasma for dynamic control of the dust therein. Future research should include 3D kinetic simulations to explore filament microstructures and extend investigations to electromagnetic cases.

#### Acknowledgments

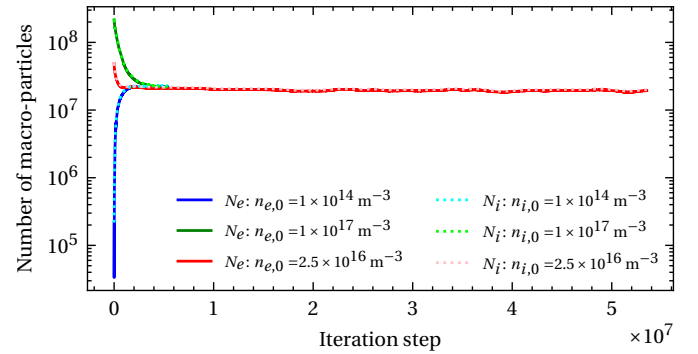
We thank Prof. L. Xu , doctoral students J.-H. Chen and B.-M. Jin , for constructive sharing of thoughts. This work is supported by the National Natural Science Foundation of

China (Grant Nos. 12305223, 12175322) and the National Natural Science Foundation of Guangdong Province (Grant No.2023A1515010762).

#### Appendix A. Supplemental cases

Authors have comprehensively analyzed the performance of argon plasma in different kinds of configurations. Plasma reactor models of varying size, different RF power supplies, effects of surface electron emissions (SEE), different initial plasma density and varying axial magnetic field strength, have been compared. Two valuable supplements are mentioned here to support our arguments. They are a comparison of different initial states (figure A1), and a case adding SEE effects (figure A2), separately.

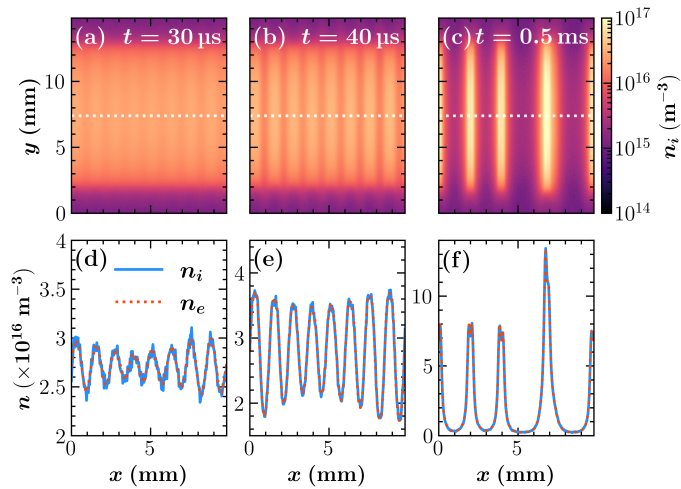
We initiated our simulations with different initial densities,  $1.0 \times 10^{14} \text{ m}^{-3}$ ,  $2.5 \times 10^{16} \text{ m}^{-3}$  and  $1.0 \times 10^{17} \text{ m}^{-3}$ , and the convergence curves are shown in figure A1. These simulations converged to nearly the same micro-particle number, demonstrating the relative independence of the final filamentary regime from the initial plasma density. This is because when the plasma discharge reaches equilibrium, the balanced plasma density and temperature are no longer relevant to the initial settings; and in our simulations, filamentation appears to commence after this equilibrium is stabilized.



**Figure A1.** Comparison of different initial states. The curves depict the temporal variations in the numbers of macro-particles throughout the simulations. These three simulations are initialized with  $n_{p,0}$  of  $1.0 \times 10^{14} \text{ m}^{-3}$ ,  $2.5 \times 10^{16} \text{ m}^{-3}$  and  $1.0 \times 10^{17} \text{ m}^{-3}$ , with the same particle weight  $w = 73728$ . The dashed curves represent the number of  $\text{Ar}^+$  macro-particles, and the solid curves represent the number of  $e^-$  macro-particles. The time step is 18.7 ps.

Figure A2 encapsulates the simulation results incorporating the SEE effects. This case differs only in the engagement of secondary electron emissions. The other simulation parameters are the same in section 2. The effect of enabling SEE is to slightly increase the electron density near the electrode, thereby maintaining the quantity of charged particles. In the SWG stage (figures A2(d-e)), the mean plasma density at half-height level reaches  $2.7 \times 10^{16} \text{ m}^{-3}$  (35% higher than mean density in figures 2(d-e)), however, the structural characteristics of the physical parameters in both sets of the cases remain consistent. The filamentary pattern observed in the ion density distribution at three selected moments exhibit limited differences to the cases





**Figure A2.** Case with SEE. Plasma population evolution within 500 microseconds. The  $\text{Ar}^+$  2D profiles present plasma distribution at distinct moments:  $t =$  (a) 30  $\mu\text{s}$ , (b) 40  $\mu\text{s}$ , (c) 500  $\mu\text{s}$ . The curves plotted in (d), (e) and (f) are the species density varying spatially along the waistline corresponding to (a–c), respectively. Typical modulational feature is presented upon the spatial waveform in (d) as well as (e).

without SEE effects. To conclude, the presence of SEE effects does not fundamentally impact the filamentation phenomena. This is consistent with the findings in [25].

## References

- [1] Zheng B, Wang K, Grotjohn T, Schuelke T and Fan Q H 2019 *Plasma Sources Sci. Technol.* **28** 09LT03
- [2] Zhang Q Z, Sun J Y, Lu W Q, Schulze J, Guo Y Q and Wang Y N 2021 *Phys. Rev. E* **104** 045209
- [3] Patil S, Sharma S, Sengupta S, Sen A and Kaganovich I D 2022 *Phys. Rev. Res.* **4** 013059
- [4] Barnat E V, Miller P A and Paterson A M 2008 *Plasma Sources Sci. Technol.* **17** 045005
- [5] Ma F F, Zhang Q Z, Cui Y M and Wang Y N 2023 *Appl. Phys. Lett.* **123** 202103
- [6] Dahiya S, Singh P, Das S, Sirse N and Karkari S K 2023 *Phys. Lett. A* **468** 128745
- [7] Fortov V E, Ivlev A V, Khrapak S A, Khrapak A G and Morfill G E 2005 *Phys. Rep.* **103**
- [8] Merlino R 2021 *Adv. Phys.: X* **6** 1873859
- [9] Melzer A, Krüger H, Maier D and Schütt S 2021 *Rev. Mod. Plasma Phys.* **5** 11
- [10] Konopka U, Schwabe M, Knapek C, Kretschmar M and Morfill G E 2005 *AIP Conf. Proc.* **799** 181–184
- [11] Schwabe M, Konopka U, Bandyopadhyay P and Morfill G E 2011 *Phys. Rev. Lett.* **106** 215004
- [12] Thomas E, Lynch B, Konopka U, Menati M, Williams S, Merlino R L and Rosenberg M 2019 *Plasma Phys. Control. Fusion* **62** 014006
- [13] Jung H, Greiner F, Piel A and Miloch W J 2018 *Phys. Plasmas* **25** 073703
- [14] Hall T and Thomas E 2020 *Phys. Rev. E* **102** 023208
- [15] Winter J 2004 *Plasma Phys. Control. Fusion* **46** B583
- [16] Krasheninnikov S I, Pigarov A Y, Smirnov R D, Rosenberg M, Tanaka Y, Benson D J, Soboleva T K, Rognlien T D, Mendis D A, Bray B D, Rudakov D L, Yu J H, West W P, Roquemore A L, Skinner C H, Terry J L, Lipschultz B, Bader A, Granetz R S, Pitcher C S, Ohno N, Takamura S, Masuzaki S, Ashikawa N, Shiratani M, Tokitani M, Kumazawa R, Asakura N, Nakano T, Litnovsky A M, Maqueda R and Group t L E 2008 *Plasma Phys. Control. Fusion* **50** 124054
- [17] Cardinaud C, Peignon M C and Tessier P Y 2000 *Appl. Surf. Sci.* **164** 72–83
- [18] Wu B, Kumar A and Pamarthy S 2010 *J. Appl. Phys.* **108** 051101
- [19] Anders A 2005 *Surf. Coat. Technol.* **200** 1893–1906
- [20] Profijt H B, Potts S E, van de Sanden M C M and Kessels W M M 2011 *J. Vac. Sci. Technol. A* **29** 050801
- [21] Thomas E, Lynch B, Konopka U, Merlino R L and Rosenberg M 2015 *Phys. Plasmas* **22** 030701
- [22] Thomas E, Konopka U, Merlino R L and Rosenberg M 2016 *Phys. Plasmas* **23** 055701
- [23] Williams S, Chakraborty Thakur S, Menati M and Thomas E 2022 *Phys. Plasmas* **29**
- [24] Kushner M J 2009 *J. Phys. D* **42** 194013
- [25] Menati M, Thomas E and Kushner M J 2019 *Phys. Plasmas* **26**
- [26] Menati M, Rasoolian B, Thomas E and Konopka U 2020 *Phys. Plasmas* **27** 022101
- [27] Menati M, Konopka U and Thomas Jr E 2021 *Contrib. Plasma Phys.* **61**
- [28] Menati M, Williams S, Rasoolian B, Thomas E and Konopka U 2023 *Commun. Phys.* **6** 1–12
- [29] Vahedi V, DiPeso G, Birdsall C K, Lieberman M A and Rognlien T D 1993 *Plasma Sources Sci. Technol.* **2** 261–272
- [30] Donkó Z 2011 *Plasma Sources Sci. Technol.* **20** 024001
- [31] Wilczek S, Schulze J, Brinkmann R P, Donkó Z, Trieschmann J and Mussenbrock T 2020 *J. Appl. Phys.* **127** 181101
- [32] Birdsall C 1991 *IEEE Trans. Plasma Sci.* **19** 65–85
- [33] Verboncoeur J P 2005 *Plasma Phys. Control. Fusion* **47** A231
- [34] Arber T D, Bennett K, Brady C S, Lawrence-Douglas A, Ramsay M G, Sircombe N J, Gillies P, Evans R G, Schmitz H, Bell A R and Ridgers C P 2015 *Plasma Phys. Control. Fusion* **57** 113001
- [35] Vahedi V and Surendra M 1995 *Comput. Phys. Commun.* **87** 179–198
- [36] Tskhakaya D, Matyash K, Schneider R and Taccogna F 2007 *Contrib. Plasma Phys.* **47** 563–594
- [37] Vahedi V and DiPeso G 1997 *J. Comput. Phys.* **131** 149–163
- [38] Charoy T, Boeuf J P, Bourdon A, Carlsson J A, Chabert P, Cuenot B, Eremin D, Garrigues L, Hara K, Kaganovich I D, Powis A T, Smolyakov A, Sydorenko D, Tavant A, Vermorel O and Villafana W 2019 *Plasma Sources Sci. Technol.* **28** 105010
- [39] Villafana W, Petronio F, Denig A C, Jimenez M J, Eremin D, Garrigues L, Taccogna F, Alvarez-Laguna A, Boeuf J P, Bourdon A, Chabert P, Charoy T, Cuenot B, Hara K, Pechereau F, Smolyakov A, Sydorenko D, Tavant A and Vermorel O 2021 *Plasma Sources Sci. Technol.* **30** 075002
- [40] Janhunens S, Smolyakov A, Sydorenko D, Jimenez M, Kaganovich I D and Raitses Y 2018 *Phys. Plasmas* **25** 082308
- [41] Sun H, Chen J, Kaganovich I D, Khrabrov A and Sydorenko D 2022 *Phys. Rev. E* **106** 035203
- [42] Xu L, Sun H, Eremin D, Ganta S, Kaganovich I D, Bera K, Rauf S and Wu X 2023 *Plasma Sources Sci. Technol.* **32** 105012
- [43] Cramer W H 1959 *J. Chem. Phys.* **30** 641–642
- [44] Banks P 1966 *Planet. Space Sci.* **14** 1085–1103
- [45] Banks P 1966 *Planet. Space Sci.* **14** 1105–1122
- [46] Sakabe S and Izawa Y 1991 *At. Data Nucl. Data Tables* **49** 257–314
- [47] Horváth B, Schulze J, Donkó Z and Derzsi A 2018 *J. Phys. D* **51** 355204
- [48] Ramos J J 2005 *Phys. Plasmas* **12** 052102
- [49] Cerri S S, Henri P, Califano F, Del Sarto D, Faganello M and Pegoraro F 2013 *Phys. Plasmas* **20** 112112
- [50] Smolyakov A I, Chapurin O, Frias W, Koshkarov O, Romadanov I, Tang T, Umansky M, Raitses Y, Kaganovich I D and Lakhin V P 2017 *Plasma Phys. Control. Fusion* **59** 014041
- [51] Nishikawa K 1968 *J. Phys. Soc. Jpn.* **24** 916–922
- [52] Nishikawa K 1968 *J. Phys. Soc. Jpn.* **24** 1152–1158
- [53] Zakharov V E 1972 *JETP* **35** 908–914
- [54] Zakharov V E, Musher S L and Rubenchik A M 1974 *JETP Lett.* **19** 151
- [55] Chen F 2016 *Introduction to Plasma Physics and Controlled Fusion* 3rd ed (Cham: Springer International Publishing)
- [56] Joshi J K, Binwal S, Karkari S K and Kumar S 2018 *J. Appl. Phys.* **123** 113301
- [57] Sun H, Chen J, Kaganovich I D, Khrabrov A and Sydorenko D 2022 *Phys. Rev. Lett.* **129** 125001
- [58] Satnoianu R A, Menzinger M and Maini P K 2000 *J. Math. Biol.* **41** 493–512
- [59] Lieberman M A and Lichtenberg A J 2005 *Principles of Plasma Discharges*

- and *Materials Processing* 2nd ed (Hoboken, N.J.: Wiley-Interscience)
- [60] Goldman M V 1984 *Rev. Mod. Phys.* **56** 709–735
- [61] Treumann R A and Baumjohann W 1997 *Advanced Space Plasma Physics* (Imperial College Press)
- [62] Jin B, Chen J, Khrabrov A V, Wang Z and Xu L 2022 *Plasma Sources Sci. Technol.* **31** 115015
- [63] Nicholson D R 1983 *Introduction to Plasma Theory* A Wiley Series in Plasma Physics (New York: Wiley)
- [64] Yang Y, Matthaeus W H, Parashar T N, Haggerty C C, Roytershteyn V, Daughton W, Wan M, Shi Y and Chen S 2017 *Phys. Plasmas* **24** 072306
- [65] Chew G F, Goldberger M L and Low F E 1956 *Proc. R. Soc. Lond. A* **236** 112–118
- [66] Cheng C Z and Johnson J R 1999 *J. Geophys. Res. Space Phys.* **104** 413–427
- [67] Maxwell J C 2010 *A Treatise on Electricity and Magnetism* 1st ed (Cambridge University Press)
- [68] Lundin R and Guglielmi A 2006 *Space Sci. Rev.* **127** 1–116
- [69] Dasgupta B, Tsurutani B T and Janaki M S 2003 *Geophys. Res. Lett.* **30**
- [70] Washimi H and Karpman V I 1976 *JETP* **44** 528–531
- [71] Tskhakaya D D 1981 *J. Plasma Phys.* **25** 233–238
- [72] Kentwell G W and Jones D A 1987 *Phys. Rep.* **145** 319–403
- [73] Ghildyal V and Kalra G L 1998 *Phys. Plasmas* **5** 390–394
- [74] Smolyakov A I, Sydorenko D and Froese A 2007 *Plasma Phys. Control. Fusion* **49** A221
- [75] Iwata N and Kishimoto Y 2013 *Phys. Plasmas* **20** 083107